

Modeling and observations of high-frequency flow variability and internal waves at a Caribbean reef spawning aggregation site

Tal Ezer · William D. Heyman · Chris Houser · Björn Kjerfve

Received: 3 August 2010 / Accepted: 30 November 2010 / Published online: 22 December 2010
© Springer-Verlag 2011

Abstract The characteristics and forcing mechanisms of high-frequency flow variations (periods of minutes to days) were investigated near Gladden Spit, a reef promontory off the coast of Belize. Direct field observations and a high-resolution (50-m grid size) numerical ocean model are used to describe the flow variations that impact the initial dispersion of eggs and larvae from this site, which serves as a spawning aggregation site for many species of reef fishes. Idealized sensitivity model experiments isolate the role of various processes, such as internal waves, wind, tides, and large-scale flow variations. The acute horizontal curvature and steep topography of the reef intensify the flow, create small-scale convergence and divergence zones, and excite high-frequency oscillations and internal waves.

Although the tides in this area are relatively small (~10-cm amplitude), the model simulations show that tides can excite significant high-frequency flow variations near the reef, which suggests that the preference of fish to aggregate and spawn in the days following the time of full moon may not be coincidental. Even small variations in remote flows ($2\text{--}5\text{ cm s}^{-1}$) due to say, meso-scale eddies, are enough to excite near-reef oscillations. Model simulations and the observations further suggest that the spawning site at the tip of the reef provides initial strong dispersion for eggs, but then the combined influence of the along-isobath flow and the westward wind will transport the eggs and larvae downstream of Gladden Spit toward less turbulent region, which may contribute to enhanced larval survival.

Responsible Editor: Huijie Xue

This article is part of the Topical Collection on *2nd International Workshop on Modelling the Ocean 2010*

T. Ezer (✉)

Center for Coastal Physical Oceanography,
Old Dominion University,
4111 Monarch Way,
Norfolk, VA 23508, USA
e-mail: tezer@odu.edu

W. D. Heyman · C. Houser
Department of Geography, Texas A&M University,
College Station, TX 77845, USA

W. D. Heyman
e-mail: wheyman@tamu.edu

C. Houser
e-mail: chouser@tamu.edu

B. Kjerfve
World Maritime University,
S-20124 Malmö, Sweden
e-mail: kjerfve@wmu.se

Keywords Numerical modeling · Internal waves · Reef promontory · Spawning aggregation · Turbulence

1 Introduction

Multispecies spawning aggregation sites along the Meso-American Barrier Reef in the western Caribbean Sea have been described in various studies (Heyman et al. 2001, 2005; Kobara and Heyman 2010). These reef promontory sites provide spawning habitat for at least 17 species of reef fishes from nine families (Heyman and Kjerfve 2008; Kobara and Heyman 2010) and exhibit a similar geomorphology over a broad geographic range (Heyman and Requena 2003; Kobara and Heyman 2010; Wright and Heyman 2008). Aggregations tend to occur at reef promontories in 20–40-m water depth near sharp shelf edges and are immediately adjacent to deep (>100 m) water. The timing and location of these spawning

aggregations are likely beneficial for species survival, but the reasons that these sites are attractive are not clear (Heyman et al. 2008). Some hypotheses suggest advantages for enhanced larval dispersal and thus survival (Barlow 1981) while other hypotheses center on offshore transport of eggs and larvae that presumably reduces egg predation by reef-based egg predators (Johannes 1978; Lobel 1978).

The focus of our study is Gladden Spit Reef off Belize (Fig. 1a) where fish aggregation events have been studied extensively over recent years. For example, Heyman et al. (2005) documented Cubera snapper spawning at the same location off the Gladden Spit Reef promontory over a 6-year period. The aggregation starts around full moon and spawning occurs usually 4–8 days after full moon in May, at sunset, and near the shelf edge at the Gladden Spit reef promontory (near the location of the instruments M1–M4 in Fig. 1b). The most common deep water currents at Gladden Spit are from north to south along the reef, but as shown by Ezer et al. (2005) and Heyman et al. (2008), the meandering of the Caribbean Current and the westward propagation of meso-scale eddies can occasionally reverse the flow near the Belize reefs. Heyman et al. (2005) described the rapid expansion of the cloud of eggs produced by the spawning (they estimated the cloud's volume to increase 30 fold within 1 min) and the drifting of the eggs north or south-westward, toward the reef, until hatching occurred (within ~20 h). In a model, the drifting eggs may be considered as passive tracers moving with the prevailing flow for about a day or so, until larvae's swimming is more significant and can reach up to ~10 km per day (Heyman et al. 2005; 2008). These observations motivate us to focus on turbulent mixing and the small-scale spatial pattern of the currents at time scales of minutes to a few days and length scales of ~10 m to ~1 km. We do not deal here with the connectivity between reefs on scales of ~10–100 km as discussed by Cowen et al. (2006); for those scales our high-resolution model will have to be coupled with larger, basin-scale models.

A numerical ocean model can be an important tool to study the flow pattern and variability near fish spawning aggregation sites and to understand the flow–topography interactions, forcing mechanisms and implications for physical-biological consequences (e.g., see Werner et al. 2007 for a review of physical-biological modeling and fish population connectivity studies). However, numerical simulation models of reef fish connectivity in the western Caribbean Sea (e.g., Ezer et al. 2005; Sheng and Tang 2004; Tang et al. 2006) often have grids that are not fine enough to resolve the initial transport fate of spawned materials from spawning aggregation sites. The relevant scale of the initial dispersion is a few meters to at most 10 to 100 s of meters compared to common model grid size

of a few kilometers. The goal here is thus to simulate the typical small-scale (10–100 s meters spatial scales) and high-frequency (minutes to hours temporal scales) variability of the flow near the reef and to investigate the impact of the particular topography of the reef. Other attempts of using high-resolution numerical models to support conservation efforts of coral reefs include for example the simulations of small-scale flows near Palau, as part of studies of the impact of climatic changes on coral bleaching (Skirving et al. 2005).

The numerical ocean model simulations with reef topography resembling Gladden Spit aim to study particular processes and forcing mechanisms, such as the role of the wind, tides and offshore currents; comparing the simulated variability of different sensitivity experiments with the measurements will tell us which forcing mechanism may be responsible for the observed variability. A similar modeling approach using sensitivity experiments with an idealized topography has previously been used to study high-resolution variability and bottom mixing of gravity currents flowing over sills (Ezer 2005, 2006); the same terrain-following generalized coordinates ocean model (Mellor et al. 2002; Ezer and Mellor 2004) is used here and in the other past studies.

Several mechanisms and forcing parameters need to be considered for the particular topography and location of the reef. Unlike many shallow coastal areas, the currents near the reef are not directly wind driven and often wind and currents are not correlated (Armstrong 2003; Heyman et al. 2008). This is partly due to the fact that the shallow reef is located immediately adjacent to the continental slope and very deep waters, such that near-reef flows are strongly connected with the deep water currents. However, the passage of weather systems, i.e., tropical waves, tropical storms, and hurricanes, across the Caribbean Sea can significantly impact the currents for short periods, as shown by the numerical simulations of Oey et al. (2007) and Sheng et al. (2007). There are currently no local meteorological observations at Gladden Spit, so satellite-derived QuikScat data (obtained from JPL/NASA) will be used to evaluate the general winds pattern in the area.

The warm surface waters during the time when aggregations occur create a strong and shallow (10–50 m) seasonal thermocline. This stratification coincides with strong bottom slopes, thus increasing the likelihood of turbulence generated by the interaction of internal waves with the topography (Legg and Adcroft 2003). The critical parameter (α) for such interaction is defined by

$$\alpha = \frac{s}{[(\omega^2 - f^2)/(N^2 - \omega^2)]^{1/2}} \quad (1)$$

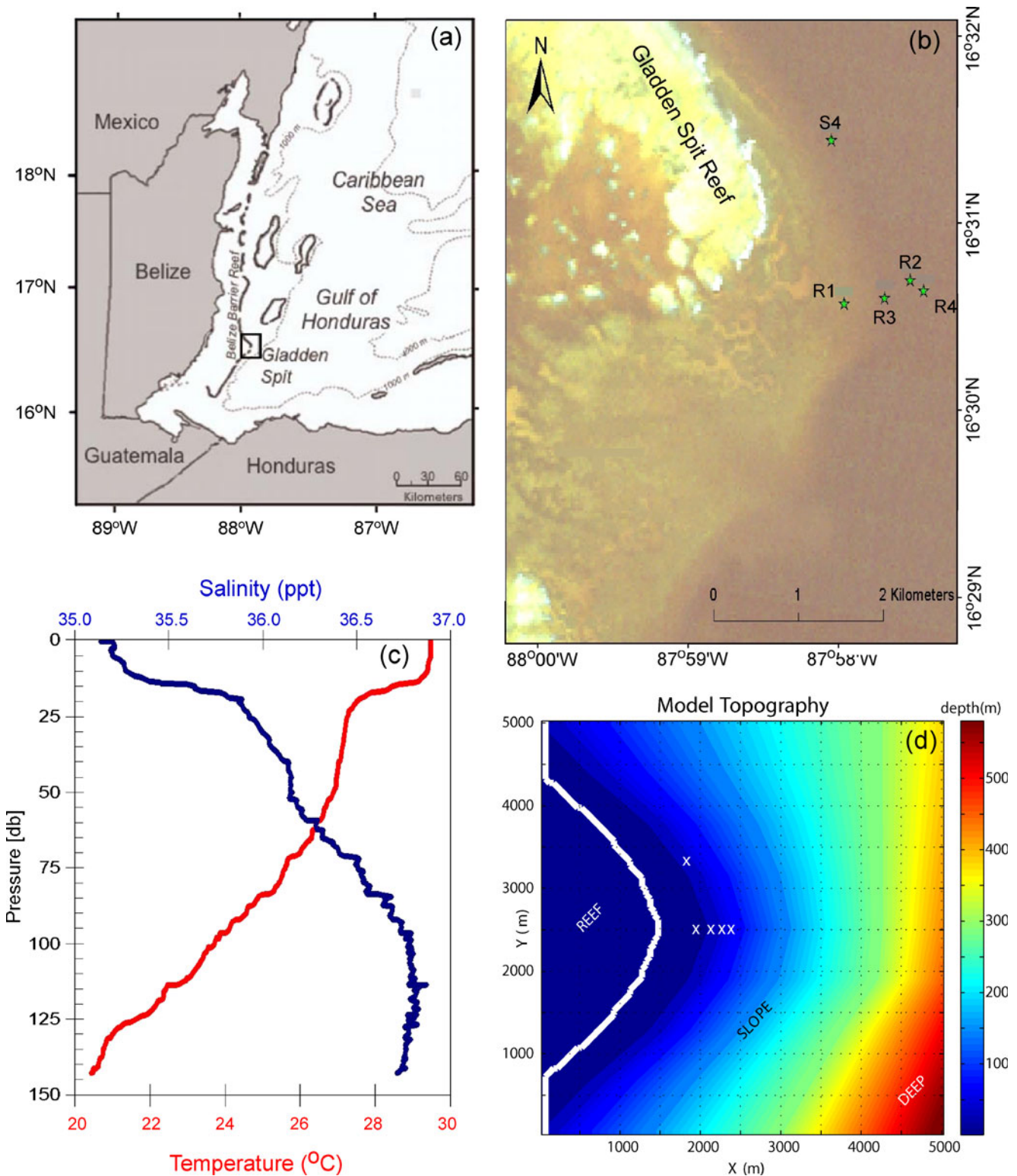


Fig. 1 **a** Map of the west Caribbean Sea region and the Gladden Spit reef. **b** Image of Gladden Spit (from Landsat TM satellite) and the location of the observations used in this study. **c** Temperature (red) and salinity (blue) profiles at Gladden Spit taken in May 1999. **d** The model domain and bottom topography. The observed temperature records at the four locations (R1–R4) at $\sim 16^{\circ}30.5'$ N and the observed

velocity record (S4) at $\sim 16^{\circ}31.5'$ N in (b) are compared with the model results at the locations indicated in (d) by “X”s. The instruments in (b) were deployed a few meters off the bottom at depths of about 10, 30, 40, and 50 m for the temperatures and about 25 m for the velocity; the model locations are approximately similar in their depths and distance from the shelf break to the observations

where s is the bottom slope, f the Coriolis parameter, g the gravity constant, ρ density and N , the Brunt–Väisälä (buoyancy) frequency, is defined by

$$N = \left[\frac{g}{\rho_o} \frac{\partial \rho}{\partial z} \right]^{1/2} \quad (2)$$

When $\alpha=1$, incoming waves with frequency ω will be reflected up and down the slope, which will lead to increased mixing and the generation of reflected waves with higher frequencies (Rattray 1960; Wunsch 1969; Garrett and Munk 1979; Eriksen 1982). Most of the known multispecies spawning aggregation sites in the Caribbean, including Gladden Spit, have convex vertical shelf edge shapes (Kobara and Heyman 2008, 2010), thus the slope s in (1) quickly changes between very small values near the reef to large values at the adjacent continental slope. Therefore, a critical vertical angle between the incoming internal waves and the slope is likely to be found in the vicinity of the shelf break for a range of frequencies, resulting in $\alpha=1$ and maximum mixing energy. Numerical simulations of internal waves reflected from slopes with various shapes show especially large increase in mixing energy for convex shaped slopes (Legg and Adcroft 2003). For the stratification in our area (Fig. 1c shows typical temperature and salinity profiles during the time of year when fish aggregations occur), the maximum frequency of internal waves, N , has a period of ~5–10 min; therefore, we analyzed model and observed records at 1-min intervals to capture the highest frequency and associated turbulent mixing. Since a hydrostatic numerical model is used here, where subgrid-scale mixing is modeled by the Mellor and Yamada (1982) turbulence scheme, the details of the internal waves are not captured as well as in a non-hydrostatic model such as that used by Legg and Adcroft (2003). Note however that mixing obtained from our hydrostatic model compares well with that obtained by non-hydrostatic models with much higher resolution, as shown by Ezer (2005). In any case, our model does provide a useful tool to study the mixing associated with the interaction of the currents with the reef topography.

Tides in the area are mixed typed, dominantly semidiurnal (mostly M_2) with relatively small amplitude of ~10 cm or less (Ezer et al. 2005) and thus at first seem to be of little influence. However, numerical simulations will show that the tides have non-negligible influence on subsurface mixing near the reef, a result that may be explained by the early work of Rattray (1960) who showed that even relatively small surface tides can generate significant internal tides and standing waves in coastal regions with large spatial variations in topography. It is interesting to note that spawning aggregations of several species occur predictably in the days after full moon at

Gladden Spit (Heyman and Kjerfve 2008) and other sites in the Caribbean (Claro and Lindeman 2003). This is intriguing and leads to the question whether the full moon serves as a visual biological trigger or if the higher spring tides at the beginning of the aggregations may confer some ecological advantage to the eggs spawned at that time, possibly increased access to food, tidal mixing, or enhancing egg dispersion.

The main goal of the study is to describe the high-frequency variability near a Caribbean reef through analysis of observations and numerical model simulations. Better understanding of the variability and physical processes may shed light on potential implications for the survival of larvae and eggs in the spawning area. In particular, the initial dispersion of eggs by turbulence and the transport of eggs by the prevailing currents during the first hours may be critical factors explaining why multispecies spawning aggregations occur so often at reefs with particular shapes.

2 Observations

2.1 Field measurements

North of the promontory, an InterOcean S4 electromagnetic current meter was moored a few meters above the bottom in ~25-m water depth (Fig. 1b). Measurements of current speed and direction, water temperature, salinity and water level were made at 2 Hz and averaged over 2 min every half hour. Additional measurements of water temperature near the bottom were measured using four RBR wave and tide gauges deployed along transect from the shelf edge to the reef edge near the bottom at depths of about 10, 30, 40, and 50 m (Fig. 1b). Temperature records averaged over 1-min intervals will be analyzed and compared with model fields output every 1 min. The first deployment of instruments was for June to December, 2009, and a second deployment of 6 months started in January, 2010. A separate study now underway will describe the seasonal variations and other long-term changes, the focus here will be on high-resolution variability within a 45-day period, June 7 to July 21, 2009. Since the variability of interest here is on scales of minutes to hours, and the sampling interval is 1 min, the analyzed period is sufficiently long enough to capture and analyze high-resolution temperature variability.

2.2 Remote sensing data

Altimeter data from the AVISO analysis (Ducet et al. 2000; <http://www.avisioceanobs.com/>) is used to evaluate the large-scale processes and forces that influence the small study area, during the period of the field measurements.

The data include a composite obtained from several satellite altimeters, daily interpolated into a $1/4^\circ \times 1/4^\circ$ box near our study site (centered around 87.75° W, 16.50° N). Sea surface height anomaly (SSHA) and derived geostrophic velocity will provide information on nearby eddies and mean circulation fields. In particular, it is interesting to know if the large-scale flow is correlated with the local observed currents, since previous studies (Ezer et al. 2005; Heyman et al. 2008) indicated that eddies have strong influence on the reef and may occasionally cause reversals of the prevailing near-reef flow. Since there are no local meteorological observations within the study area, satellite-derived QuikScat data from JPL/NASA will be used to estimate large-scale wind patterns.

2.3 Large-scale, long-term variability of currents, wind, and sea surface height

Figure 2 shows the daily variations of currents and wind from June 7 to July 21, 2009 (the period in which high-frequency variations will be analyzed). The observed currents at S4, north of the tip of the reef promontory, are predominantly southeastward, along the isobaths, and vary in speed between 0.05 to 0.25 m s^{-1} (Fig. 2a). On the other hand, the large-scale geostrophic flow is mostly flowing northwestward, parallel to the offshore Caribbean Current (Fig. 2b), generally flowing in the opposite direction of the local currents. The anomalies of both the large-scale geostrophic flow and the local currents, show variations with periods of weeks (Fig. 2c, d) which are

likely associated with offshore eddies (Ezer et al. 2005; Heyman et al. 2008). The large-scale wind (Fig. 2e) is mostly westward (easterlies, trade winds) with daily wind speeds ranging from $5\text{--}10 \text{ m s}^{-1}$. While it does seem at first look that the current variations are mostly uncorrelated with the large-scale circulation and wind, in some cases, such as the weakening of the southeastward current in July, strong westward winds at that time and its associated Ekman transport may contribute to this change. In any case, it is clear that considerable variations do occur in the large-scale circulation of the western Caribbean Sea, but the impact on the local currents is indirect and must take into account the local topography and local dynamics. The typical variations in the wind and in the large-scale flow seen here will be used later as a basis for idealized conditions that will be imposed on the numerical ocean model.

Figure 3a shows the altimeter SSHA over a 6-month period. Higher values represent warmer waters due to warm-core eddies or southward shift of the Caribbean Current and lower values (e.g., day 135) represent the presence of cold-core eddies. Local SSH is also influenced by tides that are predicted using the 5 constituents given in Ezer et al. (2005), and shown in Fig. 3b. The tides are mixed, predominantly semidiurnal (Kjerfve 1981) with the form factor at Gladden Spit, $F=(K_1+O_1)/(M_2+S_2)=(2.7+2.4)/(5.8+3.0)=0.58$. Note also the large tidal amplitude difference between Neap (2–5 cm) and Spring (10–15 cm) tide. The observed pressure (Fig. 3d) shows variations other than tides, so in Fig. 3c, the combined SSH of the

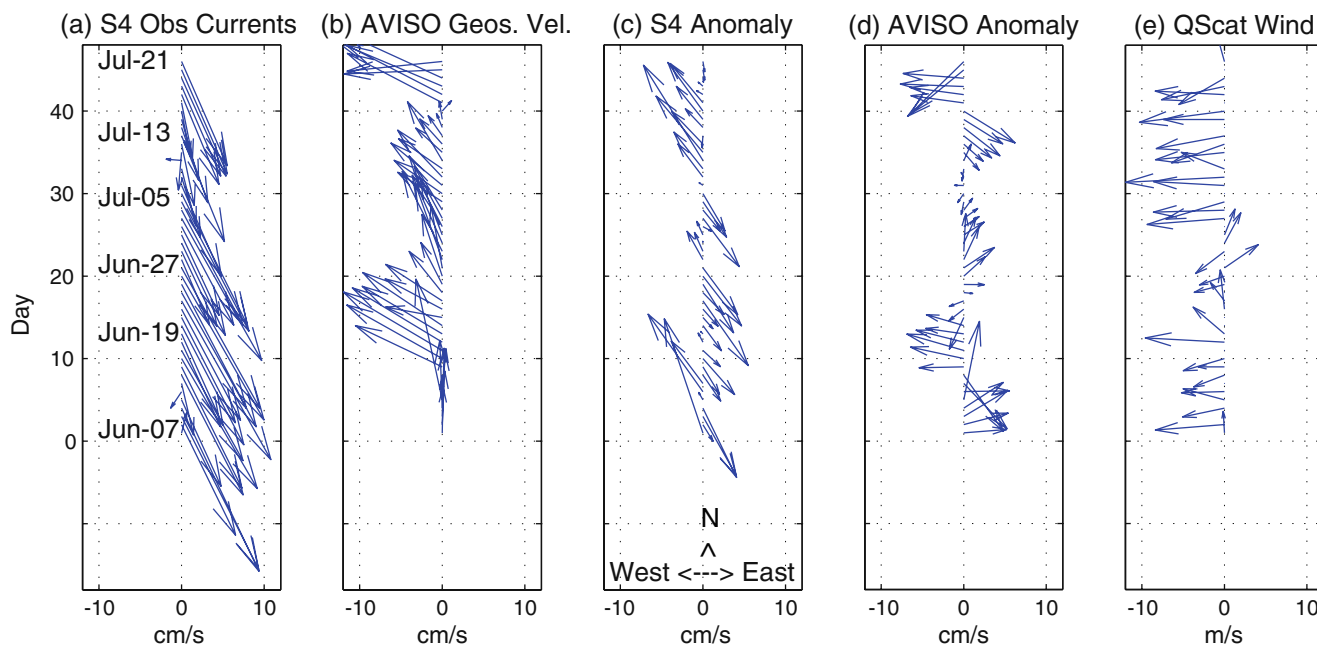
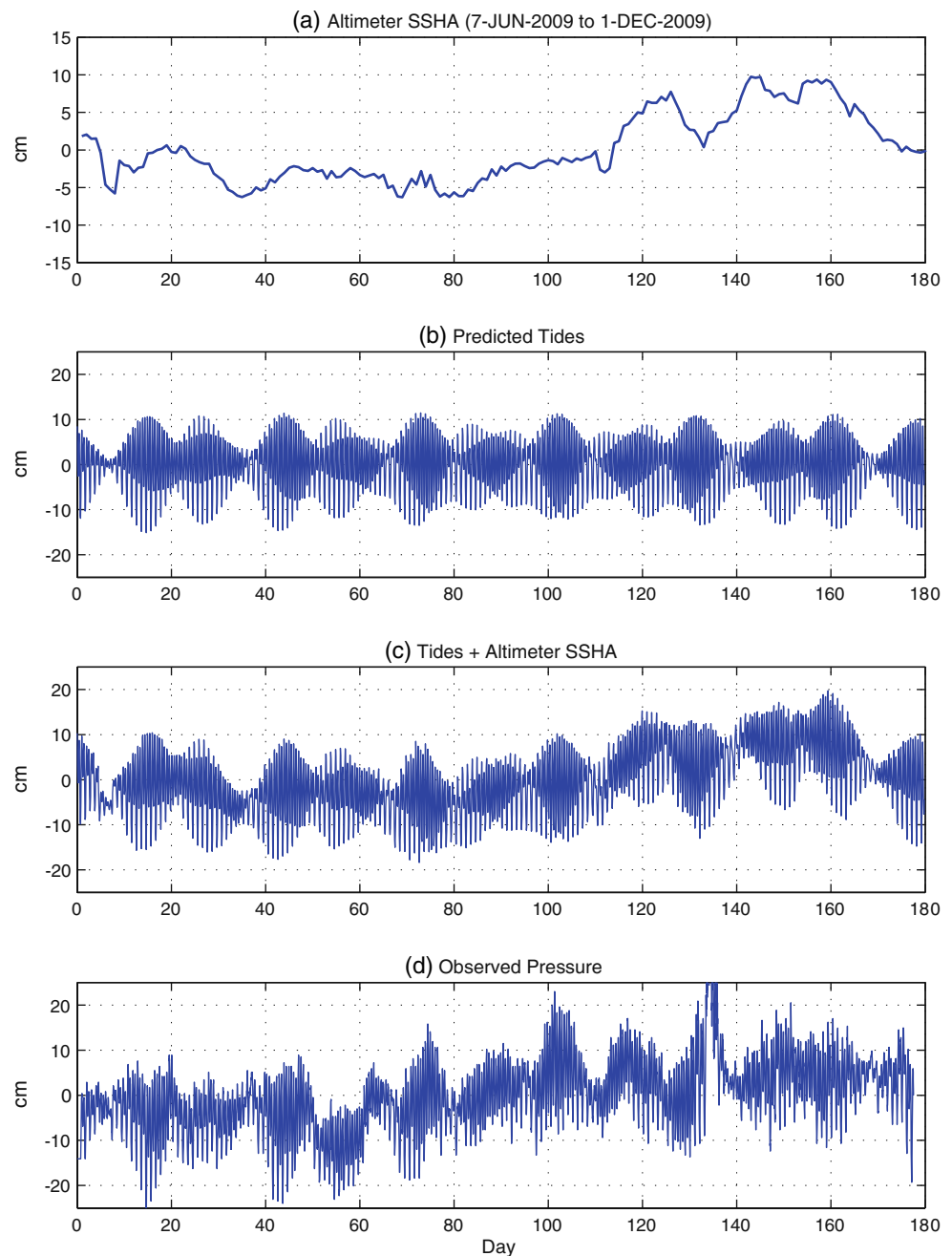


Fig. 2 Daily observations of **a** currents at S4, **b** geostrophic velocity derived from altimeter data, **c** anomaly currents of **a** relative to the mean, **d** anomaly geostrophic velocity of **b** relative to the mean, and **e** satellite-derived QuikScat winds

Fig. 3 Six-month time series of sea surface height. **a** Sea surface height anomaly (*SSHA*) from $0.25^\circ \times 0.25^\circ$ composite altimeter data near the study site (centered at 87.75° W and 16.50° N); **b** predicted tidal sea level at Gladden Spit based on the five tidal constituents given in Ezer et al. (2005); **c** tides plus *SSHA*; **d** observed water level from bottom pressure measurement at S4

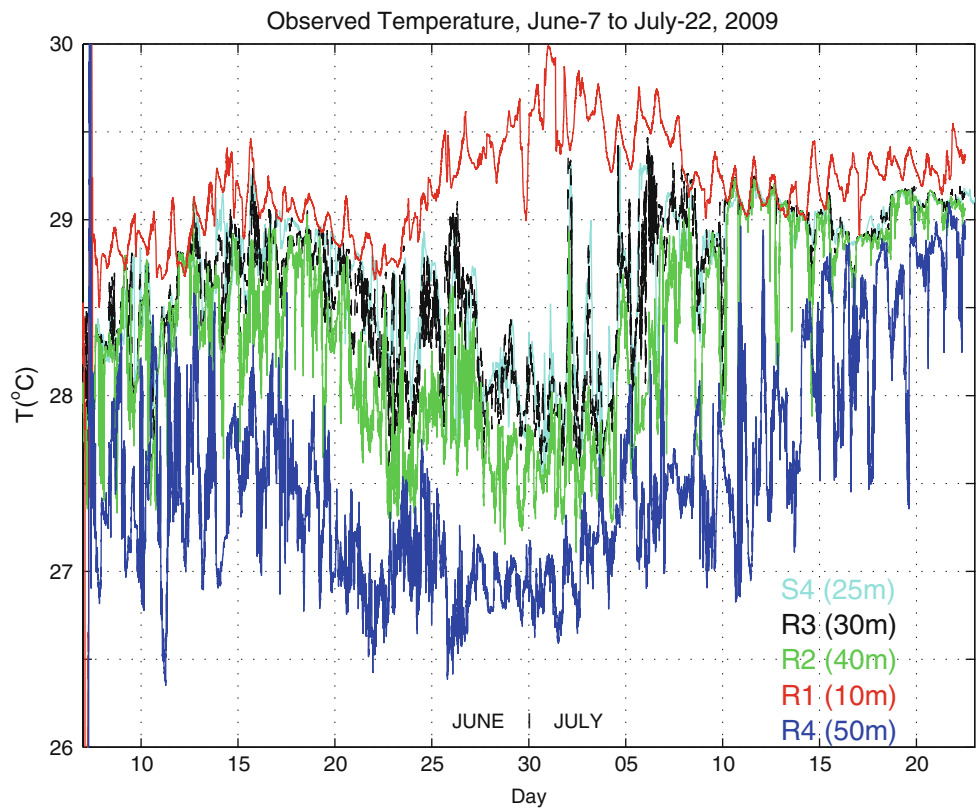


large scale from the altimeter data plus the higher frequency tides is shown to compare better with the observations than tides alone. Additional variations may be due to storm events and possibly eddies. For example, the impact of an offshore eddy (not shown) around day 135 may have caused the change in surface height (Fig. 3a) and the abnormal pressure peak (Fig. 3d). During this time, around October 21, 2009, the southeastward current was two to three times stronger than normal and the bottom temperature dropped by $\sim 2.5^\circ\text{C}$ (not shown); detail analysis of these unusual observations is left for future studies.

2.4 High-frequency oscillations of observed temperatures

After describing the general pattern of the potential large-scale forcing (eddies, wind, and tides), the focus now will shift to analysis of the local observations of near-bottom temperature variations at the five locations, four along a transect at the center of the reef (M1–M4) and one (S4) about 2 km north of the tip (Fig. 1b). Time series of temperature data recorded at 10-m depth show mostly daily variations, while those recorded between ~ 25 – 40 -m depths, showed mostly high-frequency variations (Fig. 4). In the middle of this period, from about June 25 to July 5, the

Fig. 4 Time series from June 7 to July 22, 2009, of observed temperatures at the five sites shown in Fig. 1b. The record interval is 1 min for R1–R4 and 30 min for S4



thermocline became shallower and the stratification more stable with warmer surface water at 10 m and colder water below 25-m depth. This change in temperature coincides with the shift toward weaker currents (Fig. 2a). The change in stratification (and thus N) should affect the frequency of internal waves. The highest fluctuations seen below the thermocline have periods of 5–10 min, close to the theoretical minimum period of $T=2\pi/N$ (more evidence for internal waves in the observations and the model will be presented later). To analyze the variability, an Empirical Mode Decomposition based on the Hilbert–Huang transform (HHT, Huang et al. 1998) has been applied to the data. The HHT analysis is especially useful for non-stationary processes; it divides the time series into a series of modes, but unlike a Fourier Transform where each “mode” has a constant frequency and a cosine or sine shape, the HHT allows each mode to have a time-dependent frequency and amplitude. Reconstructing all the modes together describes the distribution of variability as a function of frequency and time (Fig. 5). The analysis for the three instruments below 25 m are similar, but distinct from the 10-m record, so only analysis of the 10- and 40-m records are shown. At 10-m depth (Fig. 5a) most of the high variability is limited to periods longer than 6 h (tides, diurnal heating/cooling, etc.), with some variations at periods shorter than ~1 h (may be related to wind bursts, etc.). At 40-m depth (Fig. 5b), energetic fluctuations can be seen every few days with

periods ranging from a few minutes to a few hours. The transfer of energy between different scales by turbulence will be discussed later when observed spectrum is compared with the model. Note that during the first 7 days and the last 15 days of the record when the stratification is weaker (Fig. 4), the variability is smaller at all scales, again, pointing to the possible role that internal waves may play.

Focusing on a short period of a few hours during day 7, Fig. 6 shows an example of the first HHT mode with the highest frequencies (i.e., variations with periods longer than a few minutes are filtered out) at three locations from 30- to 50-m depth. Groups of waves seem to propagate from the deeper site to the shallower ones; it takes them ~0.5 h to move from the 30- to the 40-m site (a horizontal distance of ~220 m) and ~1 h to move from the 40- to the 30-m site (a distance of ~380 m). Therefore, the propagation speed is just over 0.1 m s⁻¹. Although there are no profiles of density taken at the time, from Fig. 4, one can estimate $N\sim 0.0125\text{ s}^{-1}$. Thus, if we assume a two-layer ocean with the top layer’s thickness about $\Delta H=10\text{ m}$, the theoretical phase speed of internal waves would be $c=[(g\Delta\rho/\rho)(\Delta H)]^{1/2}=N\Delta H=0.125\text{ m s}^{-1}$. In a continuously stratified ocean the waves will propagate in all three directions, including a vertical angle θ , so the group velocity is perpendicular to the phase velocity and has speed in the x direction of $c_g=(N/K)\sin^2\theta$, where $K=2\pi/L$ is the wave number for a wave with wavelength L . The waves seen in Fig. 6 are likely the

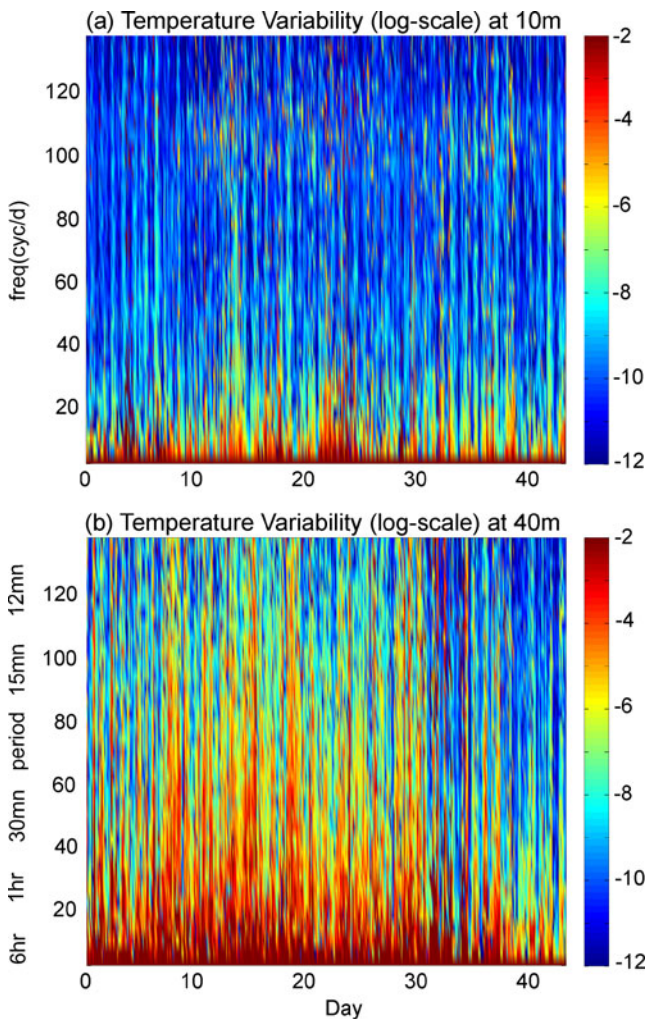


Fig. 5 Variability of temperature as a function of time and frequency for the records of Fig. 4 at **a** 10- and **b** 40-m depths. The calculations are based on the Empirical Mode Decomposition of the Hilbert spectrum (Huang et al. 1998); the units are normalized logarithmic scale with *red/blue* indicating high/low variability

result of internal waves and they have a vertical component since they seem to propagate at least between 50- and 30-m depths, but three instruments are clearly not enough to fully describe the 3D nature of the waves. More evidence of internal waves will be shown from the model simulations later.

3 Numerical modeling

3.1 The ocean model setup

The numerical ocean model used is the generalized coordinate, terrain-following ocean model of Mellor et al. (2002) which is derived from the Princeton Ocean Model. The generalized coordinate version, also used in

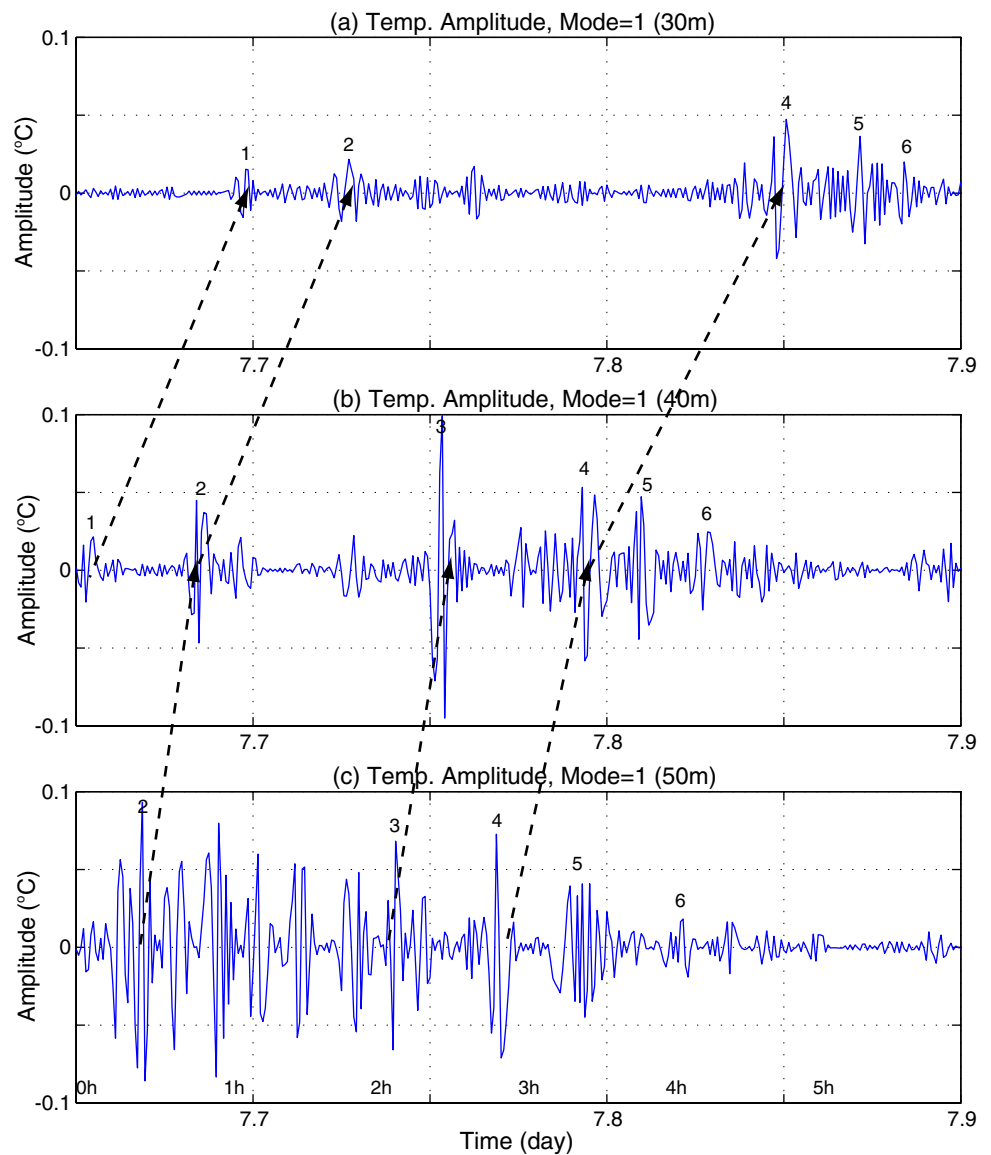
Ezer and Mellor (2004) and Ezer (2005, 2006), allows optimization of the vertical coordinate for complex topography, a feature that may be implemented in future simulations when realistic reef topography is used. In the case presented here, simple smooth bathymetry, resembling the general shape of the Gladden Spit Reef is used in a 5×5-km domain (Fig. 1d). Similar to the asymmetry found in the real reef topography (Heyman et al. 2007), slopes are steeper to the south of the reef promontory than they are to the north; however, the real rough and detailed shallow topography of the reef seen in Fig. 1b could not be simulated here. The minimum depth in the model is 5 m. Note that Gladden Spit also has a shallow reef channel (<20-m depth) that bisects the barrier reef leeward of the promontory (Fig. 1b); this feature is not included in the idealized model topography. The model used horizontal grid cells of 50×50 m and 21 vertical sigma layers, evenly distributed between the bottom and the surface. For the 50-m grid used here, the model time step for the barotropic (vertically averaged) equations was 0.2 s and for the baroclinic (three-dimensional) equations was 2 s.

There are three open boundaries in the model. A radiation condition with zero net flow is applied on the eastern boundary, while barotropic southward flow is imposed on the north and south boundaries, resembling the mean southward flow in the region. The initial condition is a spatially independent temperature and salinity, $T(z)$, $S(z)$, resembling the stratification at the beginning of the record shown in Fig. 4. There are no heat and water fluxes at the surface since the focus is on short simulations of only a few days. Because of the small domain and the imposed boundary conditions, spin up is extremely fast; it takes barotropic gravity waves a few minutes to travel the entire domain while typical currents travel the entire domain in 2–6 h. In this respect, our analyses neglect the first 5 days and neglect the 500-m area near the boundaries.

Several sensitivity experiments were conducted:

1. “No-wind” case, where wind components are nil, $U_{\text{wind}}=V_{\text{wind}}=0$, and the only forcing is a constant southward boundary flow imposed on the north and south boundaries with vertically averaged value of $U=0$, $V=-0.2 \text{ m s}^{-1}$.
2. “Variable wind” case, where an easterly wind (westward vector) of $U(t)_{\text{wind}}=-6 \text{ m s}^{-1} \pm \varepsilon(t)_{\text{wind}}$, $V_{\text{wind}}=0$, is applied, with $\varepsilon(t)_{\text{wind}}$ representing random hourly wind variations with maximum amplitude and standard deviation of 3 and 1.5 m s^{-1} , respectively. This wind is close to the typical summertime wind seen in Fig. 2. The imposed southward boundary flow is the same as in case 1.

Fig. 6 An example of a ~6-h period (day 7 of Fig. 5) of the first mode (highest frequency) of the Hilbert–Huang transform (HHT). **a–c** The observed records at 30, 40, and 50 m, respectively. *Dashed lines and numbers* indicate examples of group of waves that seem to propagate from deep to shallower water at about the speed of internal waves



3. “Variable transport” case, with no wind (as case 1), but with imposed boundary transport of $V(t) = V_{\text{mean}} \pm \epsilon_{\text{trans}}(t)$, with $V_{\text{mean}} = -0.1 \text{ m s}^{-1}$ and $\epsilon(t)_{\text{trans}}$ representing random transport variations with maximum amplitude and standard deviation of 0.05 and 0.025 m s^{-1} , respectively. These small variations represent flow variability of remote forcing outside the domain due to eddies, circulation changes, offshore storms, etc. It will be shown later that this boundary transport results in quite realistic flow variations inside the domain.
4. “Tidal forcing” case, where idealized semidiurnal tides with a period of $T = 0.5$ days (near the M_2 tide) and amplitude of $\eta_0 = 0.1 \text{ m}$ are applied on the north and south open boundaries. The barotropic tidal flow along a boundary with depth H is thus approximately $V_{\text{tide}}(x, t) = V_{\text{mean}} + \eta_0 \cos(2\pi t/T) [g/H(x)]^{1/2}$. This case represents typical conditions during Spring

Tide. In this case, $V_{\text{mean}} = -0.1 \text{ m s}^{-1}$ is the same as in case 3.

Comparisons between the various experiments and between the model and the data can tell us about the relative contribution to ocean mixing from wind variations, remote flow variations and tides. It is emphasized again that given the idealized model configuration and simplified forcing, the simulations are not expected to reproduce the observations exactly, but rather illustrate the relative importance of various forces. Nonetheless, several of the runs produce variability that is quite similar to the observations.

3.2 Sensitivity experiments and model-data comparison

Experiments 3 and 4 produce variations in the southward mean flow imposed on the model’s boundaries. The

resulting flow at ~30-m depth and ~1,700 m south of the north boundary is compared with the observations at S4 for a typical 4-day period at the middle of June during Spring Tide (Fig. 7). Note first that the model is able to correctly reproduce the direction of the flow, toward the southeast along the slope. Secondly, the mean current speed and variability in the model are intensified with values approximately twice those imposed on the boundary. The observed flow variations (Fig. 7a) include high-frequency variations with time scales of hours, similar to those in the variable transport experiment (Fig. 7b), as well as longer variations with time scales of 12 h to a few days which may include the impact of tides (Fig. 7c). Therefore, the simulated flow variability in those simplified experiments is reasonably represented, at least at this location during this time period.

The observed temperature variations near the shelf break at 30 m depth (Fig. 8a) are compared with temperatures from the different simulations (Fig. 8b–e). In experiment 1 (Fig. 8b), with constant transport, no wind and thus without any time-dependent forcing, there are only very high-frequency oscillations. Spectral analysis will show later that these oscillations are consistent with the observed high-frequency oscillations. Because all the external forcings are eliminated in this experiment, the only remaining mechanism for those small variations is the instability of the thermocline due to the vertical shear, resulting in its interface fluctuating up and down and the generation of internal waves. Adding wind variations (Fig. 8c) increases the amplitude of the temperature variations, but the result still does not resemble the observed variations (Fig. 8a), indicating that local wind is not the main forcing mechanism for flow variability in this region.

While wind does not seem to be the dominant force here, both tides and far-field ocean currents do appear to affect localized flow variability and produce large temperature fluctuations. Random remote transport variations (Fig. 8d) create abrupt temperature variations of over 0.5°C , similar to those seen in the observations (e.g., around days 45 and 90; Fig. 8a). Quite surprisingly, the idealized smooth cosine tidal forcing in experiment 4, does not result in a similar periodicity in the temperature record, but instead induces high-frequency oscillations, which are modulated by variations over longer periods (Fig. 8e). While the cooling trend and other observed variations cannot be reproduced by the simple model, the general variability is reproduced quite well in experiments 3 and 4. The results for the other instruments (not shown) are qualitatively similar to Fig. 8. Comparisons of observed and model variabilities of temperature and velocity for a 4-day period at 1-min interval sampling are summarized in Fig. 9. About 10–30% of the observed standard deviation at those short

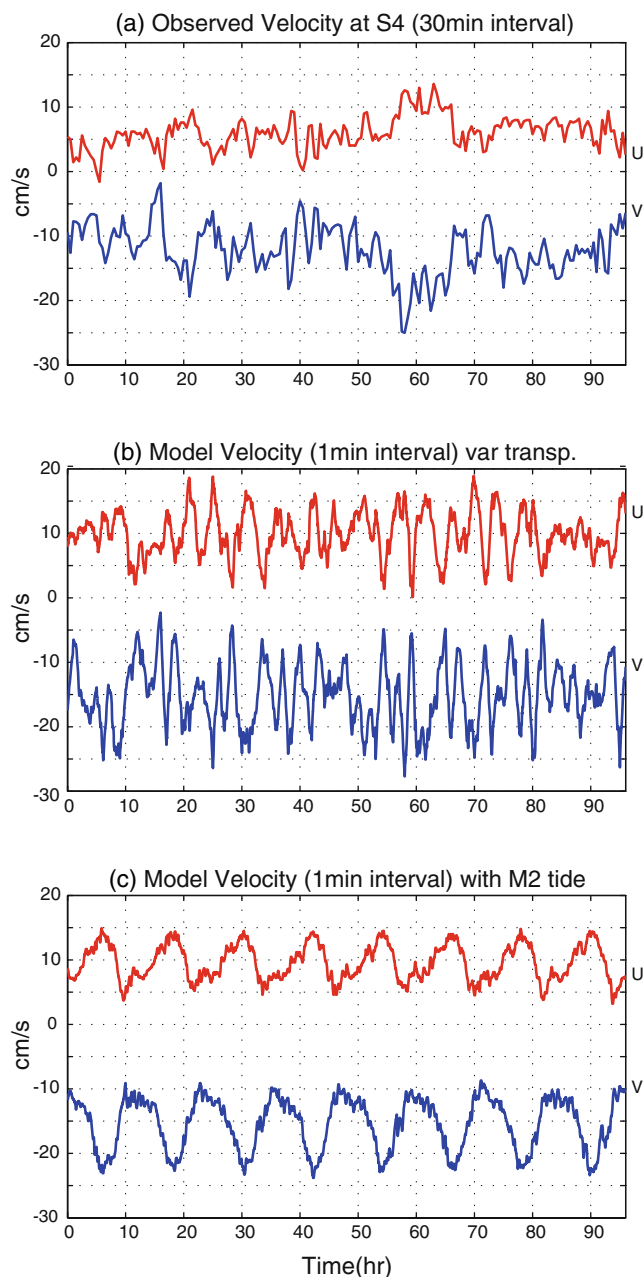
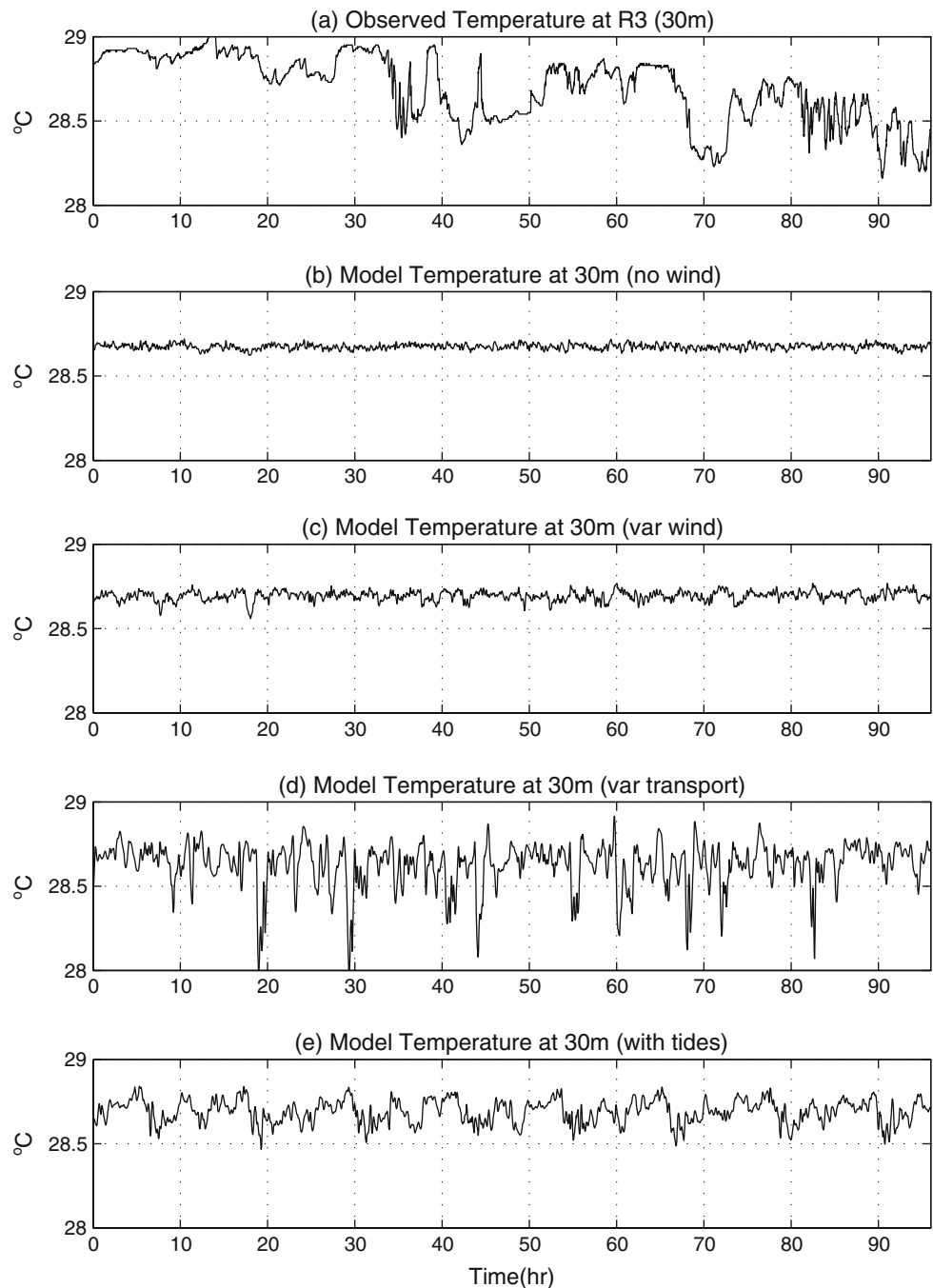


Fig. 7 Time series of 4 days of east–west (U) and north–south (V) velocity at 30-m depth: **a** observations at S4 for June 17–20, 2009, **b** model simulations with imposed boundary flow of 0.1 m s^{-1} southward transport plus random noise (maximum of ± 0.05 and standard deviation of $\pm 0.025 \text{ m s}^{-1}$), **c** model simulations with imposed boundary conditions of an M_2 -like Spring tide with amplitude of 0.1 m and a period of 12 h . Note that the observations are at 30-min intervals and the model at 1-min intervals

periods can be attributed to internal waves (experiment 1), with increased variability contributed by wind, tide and transport variations, respectively. Velocity variations (left group of bars) are quite realistic in the model if either tidal or variable transport forcing is applied.

Fig. 8 Time series of 4 days of temperature records at 30-m depth. **a** Observations at R3 for June 17–20, 2009, **b** model simulations with constant transport boundary conditions and no winds, **c** model simulations with additional westward wind of 6 m s^{-1} plus random noise, **d** model simulations with boundary conditions of transport variations, and **e** model simulations with tidal forcing



To further study the high-frequency variability in the range of periods from a few minutes to several hours (Fig. 5), spectral analysis of the observed and modeled temperatures were conducted from 4-day long-time series sampled at 1-min intervals. Analysis of longer records produced similar results. Observed (top panels of Fig. 10) and modeled results were compared for the shallowest site (10 m; left panels of Fig. 10) and the deepest site (50 m; right panels of Fig. 10). The observed records and all the model simulations show higher variability at all frequencies at 50 m than at 10 m. The $-5/3$ spectrum slope (on a log–log scale), is more evident at

50-m depth, indicating that a turbulent flow drives the temperature oscillations. In our case, for Reynolds numbers ($Re=UL/\nu$, where U , L , and ν are velocity scale, length scale and molecular viscosity, respectively) in the range $\sim 10^5$ – 10^6 , the length scale is ~ 1 – 10 m, and the flow follows that of classical turbulence (e.g., see Fig. 8.7 in Tennekes and Lumley 1972). Even for experiment 1, with no time-dependent forcing, there is a $-5/3$ slope at 50 m depth for periods between ~ 15 – 100 min (Fig. 10g), but the spectrum is flat at 10 m (Fig. 10b), indicating that the turbulence is generated where there is strong stratification, but wind is

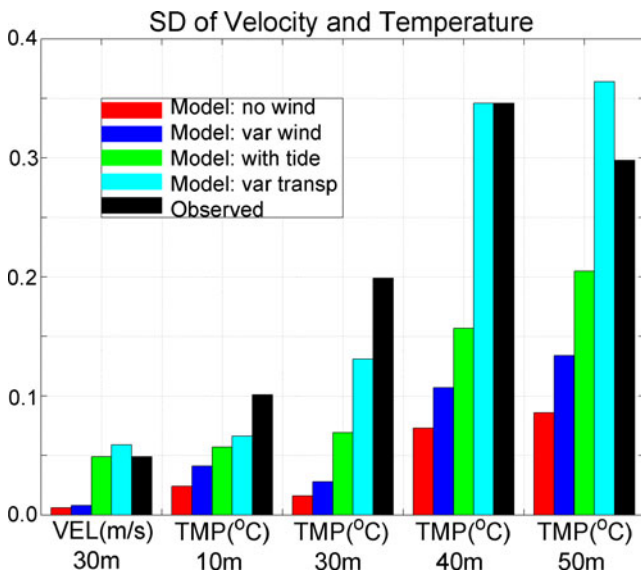


Fig. 9 The standard deviation of velocity (at 30-m depth at S4; left group of bars) and temperature (at 10-, 30-, 40-, and 50-m depth at R1–R4) for the observations (black bars) and for the four model experiments (color bars)

needed to generate turbulence near the surface. Adding wind variations does increase the variability at frequencies of 1–6 h. Tidal forcing results in the most realistic spectrum at 50 m (Fig. 10i) compared with all the other experiments, with spectrum slope a little larger than $-5/3$. At 10 m, the low frequency signal at 12 h period is evident (Fig. 10d). However, both experiments 3 and 4 (Fig. 10e) underestimate the highest variability (periods less than 15 min) at 10 m depth compared with the observations and with experiments 1 and 2. The reason is that in experiments 1 and 2 the transport was fixed with larger mean flow (-0.2 m s^{-1}) than in experiments 3 and 4 ($-0.1 \text{ m s}^{-1} \pm \varepsilon(t)$). The results thus suggest that at the shallow site turbulence was generated by velocity shear due to the bottom friction whereas shear was larger in experiments 1 and 2 due to the stronger flow. Bottom friction may also cause the discrepancy between the model and observed variability at 10-m depth, since the model does not take into account the exact rough topography of the reef (Fig. 1b).

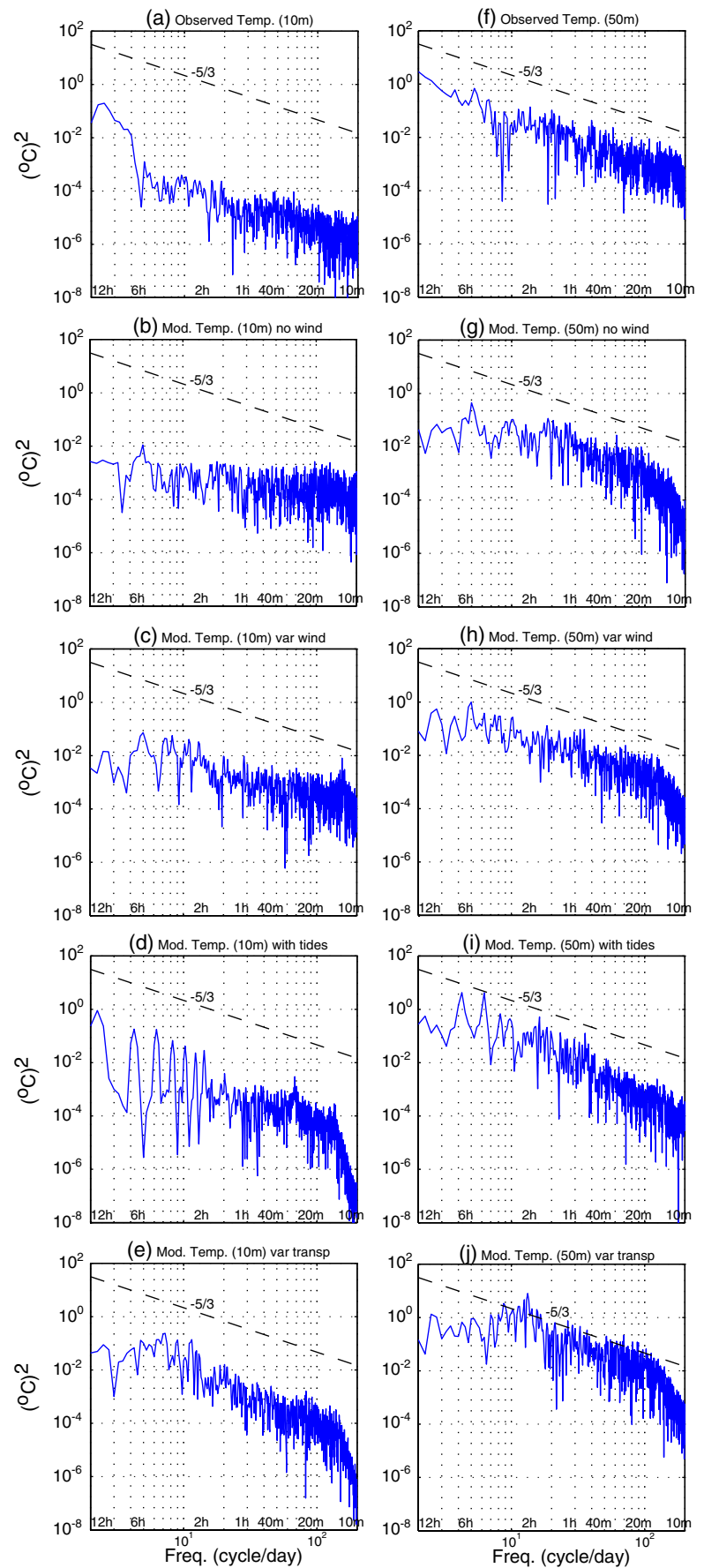
3.3 Flow–topography interactions and internal waves in the model

The interaction between the mean flow and the reef topography triggers high-frequency temperature oscillations (Fig. 10) when variations in the forcing seem relatively small- (few centimeters per second in experiments 3 and 4) or even zero (experiment 1). Fig. 11a shows that the surface velocity (experiment 1, with no forcing other than the southward constant transport) converges and intensifies along the shelf break north of the promontory, with current

speeds reaching two to three times the speed imposed on the north boundary. On the downstream side, south of the reef promontory, the strong flow is deflected away from the reef while some weak clockwise circulation occurs in shallow regions in the south. Fig. 11b shows the near-bottom flow and the divergence, $\text{DIV} = \partial u / \partial x + \partial v / \partial y$, where u and v are the velocity components at the lowest model layer above the bottom. The near-bottom flow is complicated with more organized southward flow in the northern half of the domain and more chaotic flow in the southern half of the domain. Because of the asymmetry of the topography, a deep northward return flow is generated, creating small-scale convergence and divergence zones, resulting in alternating near-bottom downwelling and upwelling at the center of the domain. This spatial upward/downward motion will uplift/deepen the thermocline and thus may trigger the generation of internal waves when flow is changing.

The interaction of the flow with topography seems to generate high-frequency oscillations. Are those variations consistent with the nature of internal waves? To answer this question, we take a closer look at the temperature variations in space and time during a short period of 12 h (Fig. 12); this period, from a model simulation with wind and transport variations, was randomly chosen and other periods look quite similar. A high variability region is found under the mixed layer, at depths between 20 and 60 m, within ~ 1 km from the shelf break, and along the bottom (Fig. 12a), which may indicate the area where incoming internal waves are reflected up and down the slope. Hovmöller diagrams of the temperature variations as a function of time and depth (Fig. 12b) and distance and time (Fig. 12c), indeed seem to indicate the propagation of internal waves. The temperature interface is fluctuating up and down in a similar fashion to classic measurements of internal waves (e.g., Eriksen 1982, various seamounts, islands and continental slopes; Hotchkiss and Wunsch 1982, Hudson Canyon; Hsu et al. 2000, the China Seas). The time scale of the fluctuations include peaks every 1–4 h, similar to the group of waves in Fig. 6, but also higher frequency oscillations with periods of 10 s to minutes (e.g., at 20 m depth on hours 4–5 in Fig. 12b), similar to those in Fig. 6. The latter high-frequency waves may not be fully resolved in the model because of its horizontal grid. The waves seem to propagate from the ocean toward the shelf break (Fig. 12c) with speeds of $\sim 0.15 \text{ m s}^{-1}$ (similar to the observations of Fig. 6) when they are more than 500 m from the shelf break, but then their speeds seem to increase near the shelf break. The wavelength of the waves is ~ 150 m, which is a reasonable value for internal waves. The results here are somewhat similar to other observations, such as those of Hotchkiss and Wunsch (1982) who measured internal waves propagating from deep waters up the Hudson submarine canyon.

Fig. 10 Spectral analysis of 4-day temperature records at 1-min interval at depth of 10 m (left) and 50 m (right). From top to bottom are the observations (a and f) and the model experiments for the cases with no wind (b and g), variable wind (c and h), tidal forcing (d and i), and transport variations (e and j)



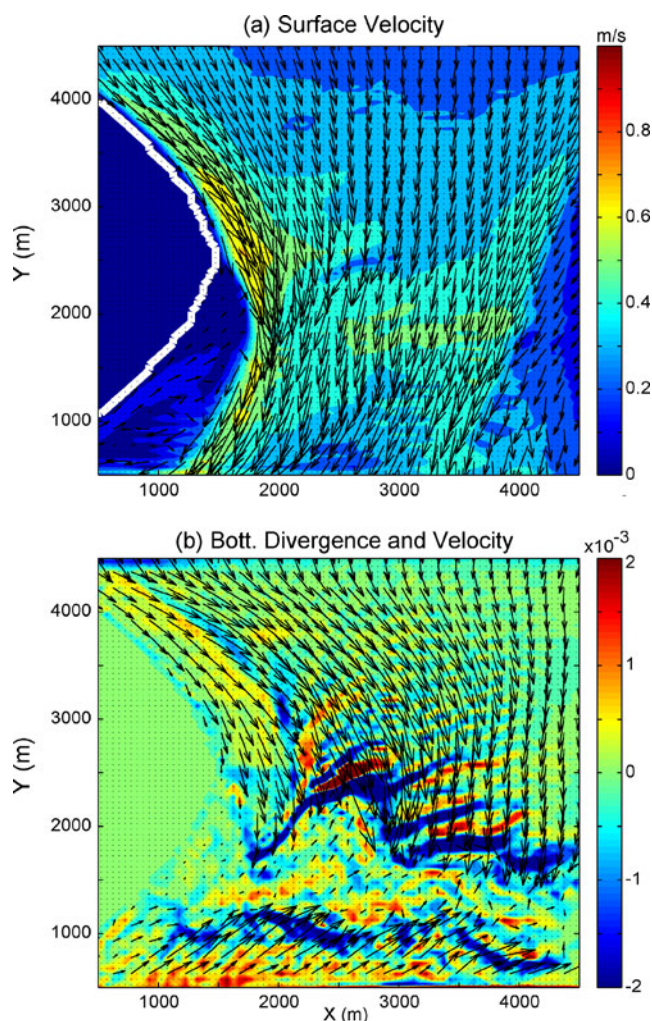


Fig. 11 Instantaneous model fields after 10 days simulation of the base experiment with no winds and no tides, driven only by a constant barotropic southward flow of 0.2 m s^{-1} at the northern boundary. **a** Surface velocity vectors and speed (*color*). **b** Bottom velocity vectors and bottom divergence (*color*, see text for details). The model domain within 500 m from the boundary is not shown

3.4 Implications for transport from the spawning area

The flow pattern around the reef will impact the initial drift of freshly fertilized fish eggs from the spawning area. To evaluate the sensitivity of this drift to southward mean flow with forcing variations, trajectories are calculated from the simulated surface flow when both wind and transport variations are included (Fig. 13). In our simulations, tidal currents will play a similar role as the transport variations experiments, with larger velocity variations during Spring tide and smaller during Neap tide. Examples of the resultant surface trajectories from the spawning area are shown in Fig. 13a–d, by releasing model drifters at the surface in an area where water depths is 10–50 m. For each of the 4 cases a different model flow is used (representing different winds and boundary transports), but the flow is assumed constant

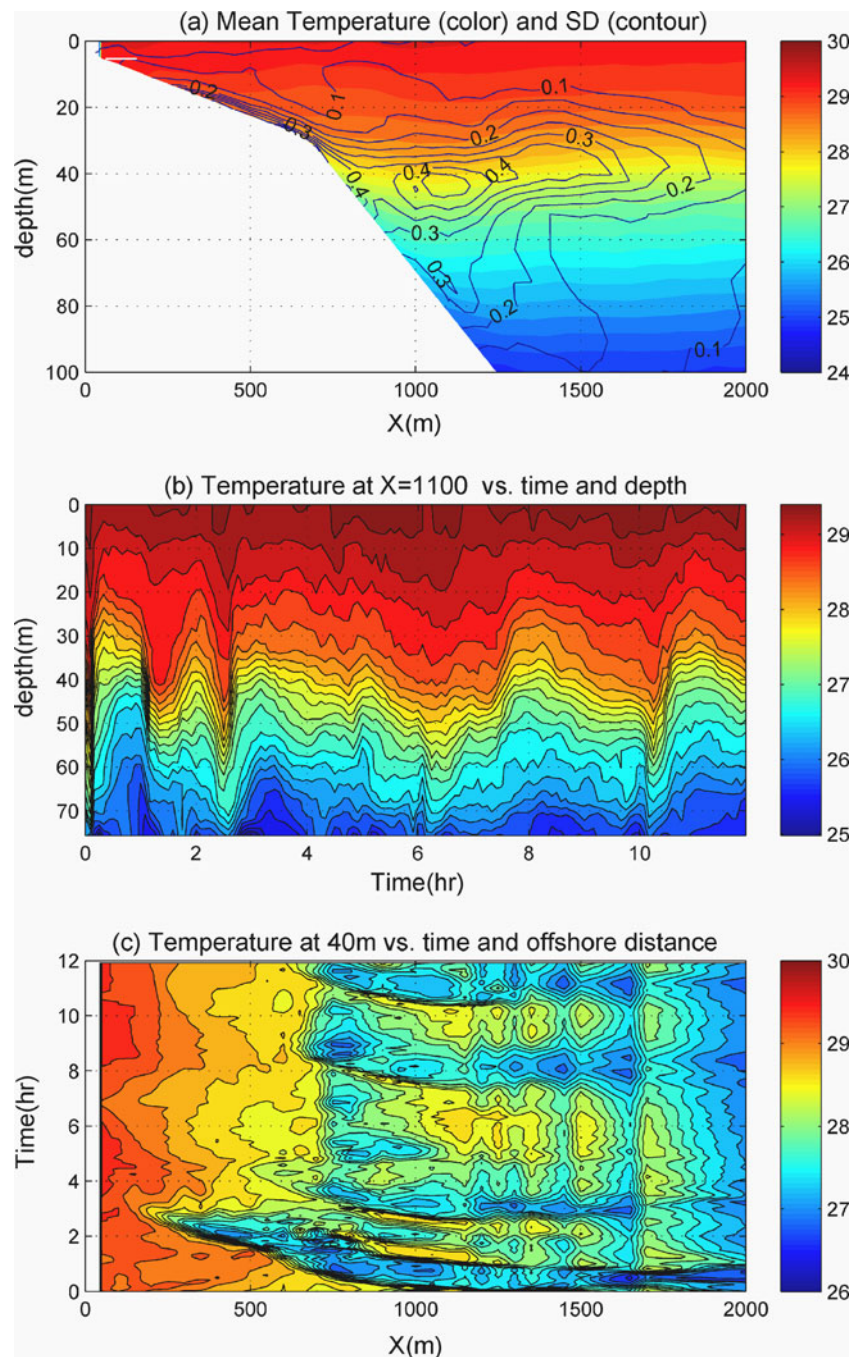
during the 1/2 h of the simulated trajectories. The most common drift direction in the model, toward the southwest is similar to the direction of most observed drifters (Fig. 13e), though occasionally drifters may move northwest with unusual wind or flow pattern. Most of the observed drifters in Fig. 13e, which moved toward the southwest, were deployed over ~3-day period (April 24–26, 2000) and stayed in the water for ~1–4 h each. During this time the winds were from the northeast or the southeast at speed of $\sim 3\text{--}6 \text{ m s}^{-1}$ and the estimated water flow speeds calculated from the distance traveled were $\sim 0.1\text{--}0.2 \text{ m s}^{-1}$, somewhat slower than the model simulated drifters. The “overnight drifter” in Fig. 13e, which moved northwestward at $\sim 0.05 \text{ m s}^{-1}$ was deployed at different time, on April 11, 2004, when the wind was similar (easterly at $\sim 5 \text{ m s}^{-1}$) to the other cases. It is obvious that the (unknown) large-scale mean flow and the influence of meso-scale eddies at the time of the drift observations in 2000 would have been completely different than at the time of the observations in 2004, thus yielding very different drift directions.

Direct comparisons between the model simulations and drifters data is left for follow-up simulations using a model with more realistic topography and forcing, but some conclusions about the trajectories behavior can be drawn from the model results. The trajectories in the model seem to be affected by two competing forces, the mean flow and the wind. On one hand, if the southward imposed mean flow is relatively weak, but the westward wind is strong, the eggs will drift toward shallower waters (Fig. 13a, b), but on the other hand, if the wind is weak and the mean flow is strong the eggs will drift toward somewhat deeper waters as the strong currents tend to “overshoot” the curved reef (Fig. 13c, d), though still not much deeper than the original depth of spawning. If the mean flow is reversed (northward, not shown) which has been demonstrated to occur when anti-cyclonic eddies impact the reef (Ezer et al. 2005), north westward drift is expected as the flow will bend around the reef in a similar, but reversed pattern to the experiments presented here. In any case, both, the observations and the model drifters indicate the tendency of the flow to bend around the curved reef and transport the eggs and larvae toward the wake of the reef. There is no indication, at least in the limited observations and idealized model presented here, that eggs will tend to drift eastward offshore into deep water currents.

4 Discussion and conclusions

Multispecies spawning aggregation sites along the Meso-American Barrier Reef in the western Caribbean Sea tend to be associated with promontories with curvature and sharp

Fig. 12 Temperature variations at the center of the domain ($Y=2,500$ m in Fig. 1c) over a 12-h period sampled every 1 min. **a** Mean east–west cross section of temperature (in color, °C) and the standard deviation (contour interval of 0.05°C). **b** Variations of temperature as a function of time and depth at $X=1,100$ m in (a). **c** Variations of temperature as a function of distance from the reef and time at depth of 40 m for $X>750$ m in (a) and at the bottom layer of the model for $0<X<750$ (where water depth is shallower than 40 m)



edges adjacent to steep slopes and deep water (Heyman et al. 2001, 2005; Heyman and Kjerfve 2008; Kobara and Heyman 2008, 2010). This suggests a survival advantage for the eggs and larvae that are dispersed in huge numbers from those locations. The first 18 h after spawning, during which time eggs disperse passively and drift with the currents may be a critical period for their survival. The eggs generally hatch in the following days to produce motile larvae which have more effect on their own destiny and are also more difficult to track. Therefore, this study aimed to understand the flow–topography interactions during the

critical initial trajectory of freshly released and fertilized eggs from reef fish spawning aggregations. To achieve this goal, observations and numerical model simulations with sampling intervals of 1 min are analyzed. Observations near the spawning locations in Gladden Spit show that there is no direct simple relation between forcing by wind and large-scale flow variations and the observed local currents (Fig. 2). However, the remote forcing may induce strong turbulence and high-frequency oscillations (periods of minutes to hours) in velocity and temperature near the spawning location near the tip of the reef. The likely

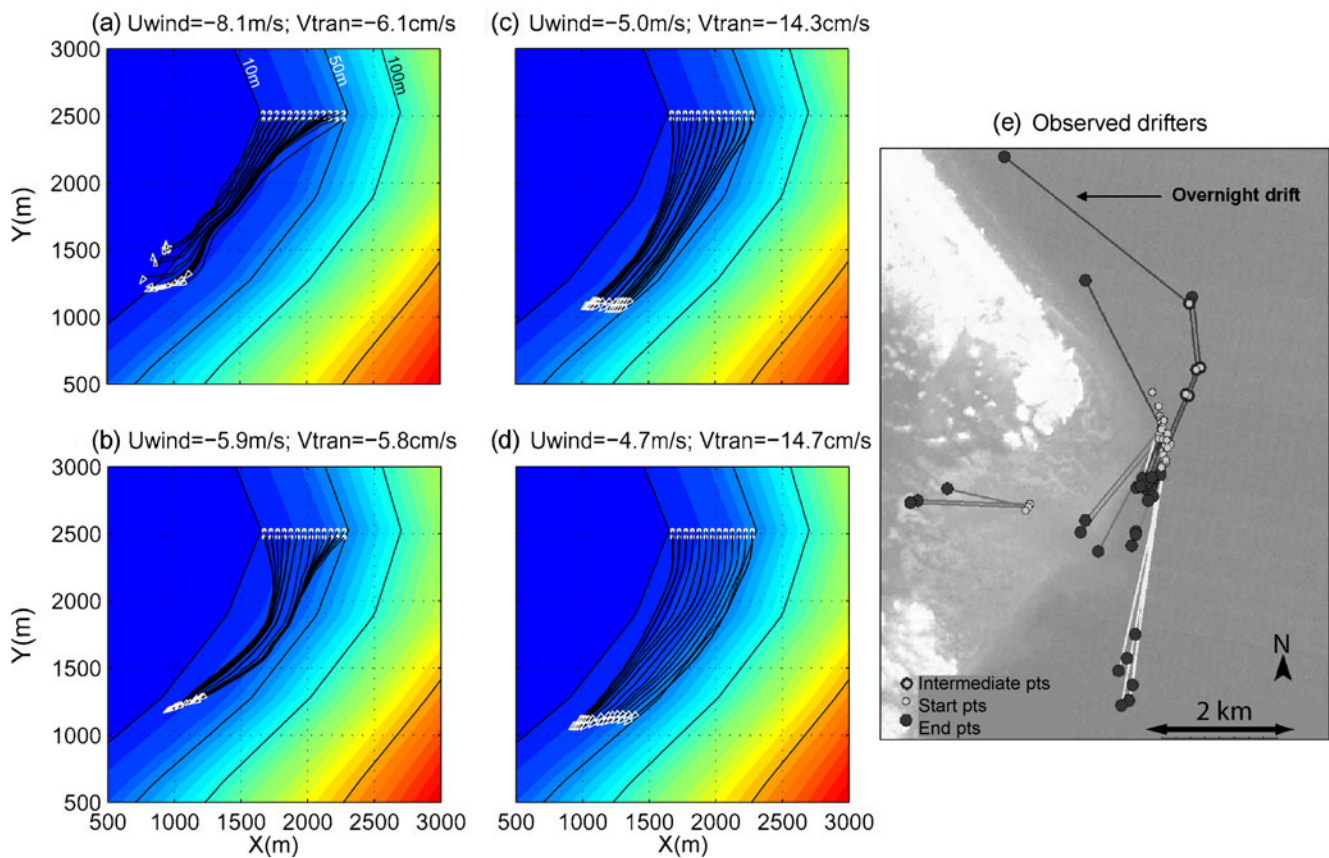


Fig. 13 a–d Bottom topography (in color) and simulated flow trajectories for half an hour after release; white dots represent the released locations and white arrowheads, the final location. The imposed wind and transport for each period are indicated; the left/right

are examples of times when the southward transport was relatively weak/strong. (e) Observed drifters released for 2–4 h at various times in Gladden Spit near the spawning site (see Heyman et al. 2008 and the text for detail)

mechanism involved here is flow–topography interactions through bottom friction and internal waves.

To identify the various mechanisms involved, sensitivity studies with a high-resolution numerical ocean model were conducted, using an idealized topography that resembles the Gladden Spit reef promontory. Each model run includes a particular process and neglects others, allowing us to evaluate the relative contributions of different forcing mechanisms on resulting flow patterns. Three particular forcing sources were tested: wind variations, tides and remote flow variations. Quite surprisingly, even in the simplest experiment with constant southward transport and no wind, high-frequency oscillations in temperature with periods of minutes to a few hours were generated below the surface mixed layer, similar to the observed oscillations in this range of frequencies (see Fig. 10f, g). Without external forcing, the mechanism suggested here for generating those oscillations is vertical motion of the isotherms due to divergence and convergence when the mean flow interacting with the topography. These variations generate internal waves that in turn generate turbulence when interacting with the bottom topography (Rattray 1960; Wunsch 1969;

Eriksen 1982; Legg and Adcroft 2003). Our hydrostatic model is not capable of resolving the details of the internal waves, but clearly suggests that they may play an important role here. Adding variable wind to the model increases the amplitude of the oscillations and generates more realistic turbulence in shallow regions, but wind variation alone does not seem sufficient to reproduce the full spectrum of the observed variations in velocity and temperature. Rather it seems that the forcing is primarily due to variations in the large-scale remote currents, either due to eddies or tides. Even small variations in the mean flow of a few centimeters per second or tidal forcing with less than 10-cm amplitude, are amplified by the shape of the reef and create variations two to three times larger than the original variations in the open ocean.

What are the implications of the study to the survival of eggs spawned at huge amounts in those reefs? Can the model shed light on plausible explanations why Caribbean fish choose reefs with particular shapes? Two issues must be considered during the first few hours after the spawning aggregation events. Firstly, the importance of the initial dispersion of the eggs, noting that Heyman et al. (2005)

described a rapid expansion of the cloud of eggs with its volume increases 30 fold within minutes. Second, the importance of the initial direction of the drift of eggs by the currents, noting that Heyman et al. (2008) and Fig 13e show the tendency of drifters to bend around the promontory, rather than move offshore. Furthermore, the trade winds generate constant swells from the east-north-east and these surface waves observed to impinge onto Gladden Spit, creating additional wave drift towards the reef. The initial dispersion and drift direction seen in the model and observations may help more eggs and larvae survive initial predation and provide a safer environment for juvenile to grow. The results confirm that the spawning site at the tip of the reef is probably the most turbulent region of the reef due to the convergence and divergence of flows there and the fact that even small variations in the mean flow (which always exist) are amplified. The turbulence at the spawning location may also enhance fertilization by mixing eggs and sperm, but further research on this hypothesis is needed.

The study suggests that the Caribbean tides, though small (Kjerfve 1981), may play a more important role than previously thought. The occurrence of spawning aggregations during the days following a full moon provides turbulent environment and large initial dispersion of eggs during the Spring Tide, but then in the following days, the tidal amplitude decreases toward the Neap Tide period, which may help the larvae and juvenile settle in the reef and survive. The model simulations also suggest that the shape of the promontory ensures that the initial transport of eggs and larvae will most likely be around the tip of the reef toward the downstream wake area that has weaker currents. This direction of the drift is affected by the local topography and probably less sensitive to changes in the mean flow or wind (Fig. 13) relative to straight coastlines. The location of the spawning sites on the eastern side of promontory reefs, coupled with the predominantly westward wind, further help assure that the drift is toward the reef and the southerly channel rather than toward the open ocean. In this respect, the spawned eggs are not entrained into larger currents resulting in long-distance transport, but rather are entrained by topographically controlled currents resulting in local transport possibly into the back reef environment.

In fish connectivity studies, there has been a growing debate about the relative role of long-distance transport of eggs and larvae from spawning sites, versus their “local retention”. These studies are often inconclusive in their results, but recent papers are favoring local retention as the predominant case with important role in the retention played by local small-scale eddies (Sponaugle et al. 2002; Paris and Cowen 2004; Werner et al. 2007). Our data analysis and model results seem to support the “local retention” hypothesis, though the interaction between the

small-scale local flow and large-scale currents needs further explorations.

The study presented here is the first step, or proof of concept demonstration, of the usage of a high-resolution numerical model to better understand the physical-biological interactions near the reef. Further studies, analyzing longer observed records, and using more realistic model configurations are clearly needed. Ideally, very high-resolution reef models should be nested within coastal ocean models which are nested within basin-scale models, so that reef connectivity can be studied from scales of a few meters to hundreds of kilometers.

Acknowledgments TE was partly supported by grants from NOAA and MMS. WH, CH, and BK were supported by grants from the Mellon Foundation, the World Bank, SDC and the Conservation International’s Marine Managed Area Science Program.

References

- Armstrong BN (2003) Currents along the Mesoamerican Barrier Reef, Western Caribbean. M.S. dissertation, University of South Carolina
- Barlow GW (1981) Patterns of parental investment, larval dispersal and size among coral reef fishes. *Environ Biol Fish* 6(1):65–85
- Claro R, Lindeman K (2003) Spawning aggregation sites of snapper and grouper species (*Lutjanidae* and *Serranidae*) on the insular shelf of Cuba. *Gulf Caribb Res* 14(2):91–106
- Cowen RK, Paris CB, Srinivasan A (2006) Scaling of Connectivity in Marine Populations. *Science* 311:522–527
- Ducet N, Le Tron PY, Reverdin G (2000) Global high-resolution mapping of ocean circulation from TOPEX/Poseidon and ERS-1 and -2. *J Geophys Res* 105:19477–19498
- Eriksen CC (1982) Observations of Internal Wave Reflection off Sloping Bottoms. *J Geophys Res* 87(C1):525–538
- Ezer T (2005) Entrainment, diapycnal mixing and transport in three-dimensional bottom gravity current simulations using the Mellor-Yamada turbulence scheme. *Ocean Model* 9(2):151–168
- Ezer T (2006) Topographic influence on overflow dynamics: Idealized numerical simulations and the Faroe Bank Channel overflow. *J. Geophys Res* 111 (C02002), doi:10.1029/2005JC003195
- Ezer T, Mellor GL (2004) A generalized coordinate ocean model and a comparison of the bottom boundary layer dynamics in terrain-following and in z-level grids. *Ocean Model* 6(3–4):379–403
- Ezer T, Thattai DV, Kjerfve B, Heyman WD (2005) On the variability of the flow along the Meso-American Barrier Reef system: a numerical model study of the influence of the Caribbean current and eddies. *Ocean Dyn* 55:458–475
- Garrett C, Munk W (1979) Internal waves in the ocean. *Ann Rev Fluid Mech* 11(A79-24751 09-34):339–369
- Heyman WD, Graham RT, Kjerfve B, Johannes RE (2001) Whale sharks *Rhincodon typus* aggregate to feed on fish spawn in Belize. *Mar Ecol Prog Ser* 215:275–282
- Heyman WD, Requena N (2003) Fish spawning aggregation sites in the MBRS region: Recommendations for monitoring and management. MBRS Technical Document No. 16, Mesoamerican Barrier Reef System Project, Belize City, Belize, 49p (available from The Nature Conservancy, Arlington, Virginia; www.conserveonline.org)
- Heyman WD, Kjerfve B, Graham RT, Rhodes KL, Garbutt L (2005) Spawning aggregations of *Lutjanus cyanopterus* (Cuvier) on the Belize Barrier Reef over a 6 year period. *J Fish Biol* 67(1):83–101

- Heyman WD, Ecochard JB, Biasi FB (2007) Low-cost bathymetric mapping for tropical marine conservation—a focus on reef fish spawning aggregation sites. *Mar Geodesy* 30(1):37–50
- Heyman WD, Kjerfve B, Ezer T (2008) Mesoamerican reef spawning aggregations help maintain fish populations: a review of connectivity research and priorities for science and management. In: Grober-Dunsmore R, Keller BD (eds) *Marine Sanctuaries Conservation Series ONMS-08-07*. NOAA, Silver Spring, pp 150–169
- Heyman WD, Kjerfve B (2008) Characterization of transient multi-species reef fish spawning aggregations at Gladden Spit, Belize. *Bull Mar Sci* 83(3):531–551
- Hotchkiss FS, Wunsch C (1982) Internal waves in Hudson Canyon with possible geological implications. *Deep Sea Res* 29(4):415–442
- Hsu M-K, Liu AK, Liu C (2000) A study of internal waves in the China Seas and Yellow Sea using SAR. *Cont Shelf Res* 20(4–5):389–410
- Huang NE, Shen Z, Long SR, Wu MC, Shih EH, Zheng Q, Tung CC, Liu HH (1998) The Empirical Mode Decomposition and the Hilbert spectrum for nonstationary time series analysis. *Proc R Soc Lond* 454:903–995
- Johannes RE (1978) Reproductive strategies of coastal marine fishes in the tropics. *Environ Biol Fish* 3:65–84
- Kjerfve B (1981) Tides of the Caribbean Sea. *J Geophys Res* 86 (C5):4243–4247
- Kobara S, Heyman WD (2008) Geomorphometric patterns of Nassau grouper (*Epinephelus striatus*) spawning aggregation sites in the Cayman Islands. *Mar Geodesy* 31:231–245
- Kobara S, Heyman WD (2010) Sea bottom geomorphology of multi-species spawning aggregation sites in Belize. *Mar Ecol Prog Ser* 405:243–254
- Legg S, Adcroft A (2003) Internal wave breaking at concave and convex continental slopes. *J Phys Oceanogr* 33:2224–2246
- Lobel PS (1978) Diel, lunar, and seasonal periodicity in the reproductive behavior of the pomacanthid fish, *Centropyge potteri*, and some other reef fishes in Hawaii. *Pac Sci* 32:193–207
- Mellor GL, Yamada T (1982) Development of a turbulent closure model for geophysical fluid problems. *Rev Geophys* 20:851–875
- Mellor GL, Hakkinen S, Ezer T, Patchen R (2002) A generalization of a sigma coordinate ocean model and an intercomparison of model vertical grids. In: Pinardi N, Woods JD (eds) *Ocean forecasting: conceptual basis and applications*. Springer, New York, pp 55–72
- Oey L-Y, Ezer T, Wang D-P, Yin X-Q, Fan S-J (2007) Hurricane-induced motions and interaction with ocean currents. *Cont Shelf Res* 27:1249–1263
- Paris CB, Cowen RK (2004) Direct evidence of a biophysical retention mechanism for coral reef fish larvae. *Limn Oceanogr* 49(6):1964–1979
- Rattray M (1960) On the coastal generation of internal tides. *Tellus* 12 (1):54–62
- Sheng J, Tang L (2004) A two-way nested-grid ocean circulation model for the Meso-American Barrier Reef System. *Ocean Dyn* 54:232–242
- Sheng J, Wang L, Andréfouët S, Hu C, Hatcher BG, Muller-Karger FE, Kjerfve B, Heyman WD, Yang B (2007) Upper ocean response of the Mesoamerican Barrier Reef System to Hurricane Mitch and coastal freshwater inputs: a study using sea-viewing wide field-of-view sensor (SeaWiFS) ocean color data and a nested-grid ocean circulation model. *J Geophys Res* 112 (C07016), doi:10.1029/2006JC003900
- Skirving WJ, Heron SF, Steinberg CR, Strong AE, McLean C, Heron ML, Choukroun SM, Arzayus LF, Bauman LG (2005) “Palau modeling final report”. National Oceanic and Atmospheric Administration and Australian Institute of Marine Sciences, Townsville. p. 46.
- Sponaugle S, Cowen RK, Shanks A, Morgan SG, Leis JM, Pineda J, Boehlert GW, Kingsford MJ, Lindeman KC, Grimes C, Munro JL (2002) Predicting self-recruitment in marine populations: biophysical correlates and mechanisms. *Bull Mar Sci* 70(Suppl 1):341–375
- Tang L, Sheng J, Hatcher BG, Sale PF (2006) Numerical study of circulation, dispersion, and hydrodynamic connectivity of surface waters on the Belize shelf. *J Geophys Res* 111 (C01003), doi:10.1029/2005JC002930
- Tennekes H, Lumley JL (1972) *A first course in turbulence*. MIT Press, Cambridge, p 300
- Werner FE, Cowen RK, Paris CB (2007) Coupled biological and physical models: present capabilities and necessary developments for future studies of population connectivity. *Oceanography* 20 (3):54–69
- Wright DJ, Heyman WD (2008) Introduction to the special issue: marine and coastal GIS for geomorphology, habitat mapping and marine reserves. *Mar Geodesy* 31:1–8
- Wunsch C (1969) Progressive internal waves on slopes. *J Fluid Mech* 35:131–145